

Full characterization of measurement-induced transitions of a superconducting qubit

Thomas Connolly,^{1,*} Pavel D. Kurilovich,^{1,*} Vladislav D. Kurilovich,^{1,†} Charlotte G. L. Böttcher,^{1,‡}
Sumeru Hazra,¹ Wei Dai,¹ Andy Z. Ding,¹ Vidul R. Joshi,^{1,§} Heekun Nho,¹ Spencer Diamond,¹
Daniel K. Weiss,^{1,2,¶} Valla Fatemi,^{1,3} Luigi Frunzio,¹ Leonid I. Glazman,^{1,2} and Michel H. Devoret^{1,**}

¹*Departments of Applied Physics and Physics, Yale University, New Haven, Connecticut 06520, USA*

²*Yale Quantum Institute, Yale University, New Haven, Connecticut 06511, USA*

³*School of Applied and Engineering Physics, Cornell University, Ithaca, New York 14853, USA*

Repeated quantum non-demolition measurement is a cornerstone of quantum error correction protocols [1, 2]. In superconducting qubits, the speed of dispersive state readout can be enhanced by increasing the power of the readout tone. However, such an increase has been found to result in additional qubit state transitions that violate the desired quantum non-demolition character of the measurement [3, 4]. Recently, the readout of a transmon superconducting qubit was improved by using a tone with frequency much larger than the qubit frequency [5]. Here, we experimentally identify the mechanisms of readout-induced transitions in this regime. In the dominant mechanism, the energy of an incoming readout photon is partially absorbed by the transmon and partially returned to the transmission line as a photon with lower frequency. Other mechanisms involve the excitation of unwanted package modes, decay via material defects [6], and, at higher qubit frequencies, the activation of undesired resonances in the transmon spectrum [3, 7]. Our work provides a comprehensive characterization of superconducting qubit state transitions caused by a strong drive.

I. INTRODUCTION

Measurement is a central operation in quantum computation, forming the basis of quantum error correction protocols [1, 2, 8–11]. In these protocols, a high-fidelity measurement must be applied to the same qubit repeatedly, for many subsequent cycles of error correction. Therefore, in addition to being precise, the measurement should also leave the observed state intact, i.e., present a quantum non-demolition (QND) character. In circuit quantum electrodynamics, an approximation to QND measurement is achieved by dispersive readout [12–21], see Figure 1(a,b). In this readout scheme, the qubit state is inferred from the non-resonant microwave tone elastically scattered off the qubit through the readout resonator.

Dispersive readout has to be performed much faster than the qubit relaxation time [22]. Shortening the duration of the measurement necessitates increasing the power of the probe tone to maintain the same signal-to-noise ratio. However, increasing the power of the tone has been found to induce unwanted transitions between the qubit states that diminish the QND character of the

measurement. These drive-induced transitions can occur from one computational state to another [6, 23–26] or from a computational state to a non-computational state [3, 4, 16, 18, 26–28]. The latter type of transitions – “leakage” from the computational subspace – is especially problematic. Leakage can lead to the loss of control over the qubit state and thus decapitate quantum error correction protocols [29–37]. For transmon qubits, one of the dominant mechanisms of leakage is the activation of accidental multi-excitation resonances in the transmon spectrum involving non-computational states [3, 7, 38–41].

Raising the frequency of the readout tone to well beyond the frequency of the transmon allows one to avoid activating multi-excitation resonances. The advantages of such an off-resonant readout were demonstrated in our previous work [5]. We achieved a QND fidelity above 99.9% by using a readout resonator with a frequency 12 times higher than that of the transmon. However, the performance of such a high-frequency readout could not be further improved by increasing the power. This raises the question of the mechanisms that limit the QND fidelity of the readout.

In this work, we experimentally identify the mechanisms that violate the QND nature of the high-frequency readout, where $\omega_{\text{res}} \gg \omega_q$ (ω_{res} and ω_q are frequencies of the readout resonator and the qubit, respectively). The leading leakage mechanism is similar to the well-known Raman scattering of light: a readout photon incoming from the transmission line is “split” between a qubit excitation and an outgoing photon at a lower frequency, see Figure 1(c,d). We identify this inelastic scattering process by measuring the rates of unwanted transmon state transitions, and comparing these rates to the parameter-free theory which we develop.

According to the theory, when the drive photon scat-

* These two authors contributed equally.
tom.connolly@yale.edu, pavel.kurilovich@yale.edu

† Present address: Google Quantum AI, 301 Mentor Dr, Goleta, CA93111, USA

‡ Present address: Department of Applied Physics, Stanford University, Stanford, California 94305, USA

§ Present address: Microsoft Quantum

¶ Present address: Quantum Circuits, Inc., New Haven, CT, USA
michel.devoret@yale.edu

** Present address: Physics Dept., U.C. Santa Barbara, Santa Barbara, California 93106, USA and Google Quantum AI, 301 Mentor Dr, Goleta, California 93111, USA

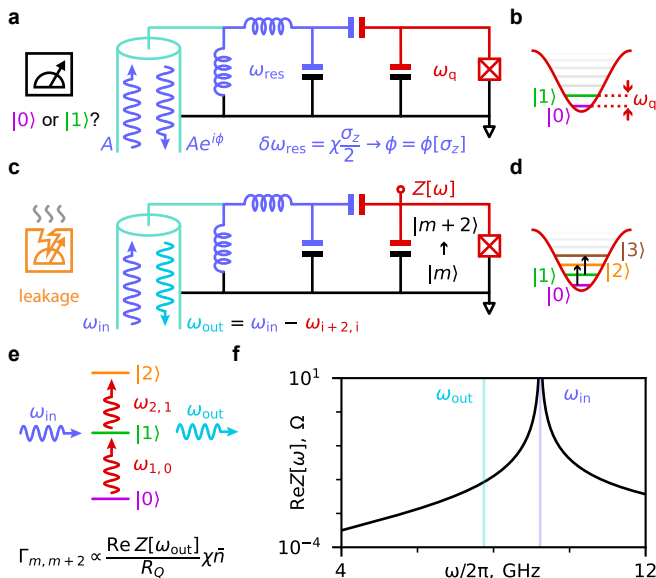


Figure 1. Transmon state transitions caused by inelastic scattering of drive photons. (a) Dispersive readout of a transmon qubit is achieved by elastically scattering microwave photons off the readout resonator coupled to the qubit. Since the resonator frequency depends on the qubit state, the phase of the reflected signal can be used to infer whether the state is $|0\rangle$ or $|1\rangle$. Dispersive shift χ quantifies the difference of resonator frequencies for the two computational states. (b) Level diagram of the transmon. Colored horizontal lines show computational states while grey lines show non-computational states. (c) Due to the transmon non-linearity, readout photons with frequency ω_{in} can scatter inelastically by giving off part of their energy to the qubit and producing a photon at a lower frequency ω_{out} . This process leads to the leakage error where transmon prepared in a computational state $|0\rangle$ excites to state $|2\rangle$. Similar process leads to excitation $|1\rangle \rightarrow |3\rangle$. (d) Schematic of the leakage process mediated by inelastic scattering. (e) Inelastic scattering is governed by a four-wave mixing non-linearity of the transmon. The rate of inelastic scattering is proportional to the drive power, quantified by the number of photons in the resonator \bar{n} . It is also proportional to the dissipative part of the impedance $Z[\omega]$ of the transmon island evaluated at the frequency ω_{out} . Here, $R_Q = h/e^2 \approx 25.8\text{k}\Omega$ is the resistance quantum. (f) Dissipative part of the impedance $Z[\omega]$ computed with lumped-element model of panel (a).

ters inelastically off the transmon, the latter excites to a non-computational state, see Figure 1(e,f). We show that the strongest processes of this type are $|0\rangle \rightarrow |2\rangle$ and $|1\rangle \rightarrow |3\rangle$, where $|m\rangle$ denotes the m -th eigenstate of the transmon. We independently measure the rates of such transitions and show that they are in agreement with the theory. As expected, the rate of unwanted transitions is proportional to the power of the readout tone. The proportionality coefficient is sensitive to the electromagnetic environment of the transmon at the frequency of outgoing photons ω_{out} . This frequency is different from both the qubit frequency ω_q and the readout frequency ω_{res} . Undesired transitions can thus be suppressed by

engineering the readout channel to reduce dissipation at frequency ω_{out} .

The described above inelastic scattering process, tied to the readout channel itself, is only one of the possible mechanisms that violate the QND character of the measurement. By changing the qubit frequency, we resolve additional demolishing processes. They correspond to accidental resonances with spurious modes either in the electromagnetic environment or the materials of the device [6]. Due to these resonances, the rate of undesired state transitions becomes elevated at a discrete set of qubit frequencies. At the highest achievable qubit frequencies, we also witness the onset of transitions caused by the multi-excitation resonances between the computational and non-computational states.

Our experimental and theoretical results paint a complete picture of measurement-induced state transitions caused by the dispersive readout of a superconducting qubit. The mechanisms of state transitions that we uncover are also relevant for other contexts where a strong off-resonant drive is applied to the transmon. These include parametric gates [42–44] and quantum control of linear oscillators [10, 45].

II. MEASURING THE TRANSITION RATES

We begin by describing the details of our experimental system. It consists of a transmon qubit and a readout resonator implemented in a 2D architecture, see Figure 2(a,b). The transmon has charging energy $E_C/h = 36$ MHz; its frequency can be tuned between $\omega_q/2\pi = 0.520$ GHz and $\omega_q/2\pi = 1.53$ GHz with magnetic flux through a SQUID loop. Our recent readout result [5] was obtained with this device tuned to a frequency $\omega_q/2\pi = 0.758$ GHz (corresponding to magnetic flux $\Phi \approx 0.42\Phi_0$, where Φ_0 is the flux quantum). A quarter-wave readout resonator has frequency between $\omega_{\text{res}}/2\pi = 9.223$ GHz and $\omega_{\text{res}}/2\pi = 9.240$ GHz depending on the transmon flux bias. The resonator linewidth is $\kappa/2\pi = 1.80$ MHz. The linewidth is determined by the inductive coupling of the resonator to the readout transmission line. At the bias point of Ref. [5], the strength of capacitive coupling between the qubit and the resonator is $g/2\pi = 515$ MHz. The presence of the transmon results in the state-dependent pull of the cavity frequency. For example, at $\omega_q/2\pi = 0.758$ GHz, the difference between the frequency shifts with transmon being in its ground or excited state is $\chi/2\pi = 0.90$ MHz, allowing us to readout the transmon state.

To probe the the unwanted transitions caused by the drive, we initialize the transmon in either its ground state $|0\rangle$ or in its excited state $|1\rangle$. We then apply a pulsed tone at a frequency ω_{in} close to that of the readout resonator. We detune the drive by many resonator linewidths to suppresses the measurement-induced broadening of qubit transitions (by 40 to 55 MHz depending on the flux bias). This simplifies the analysis of drive-induced tran-

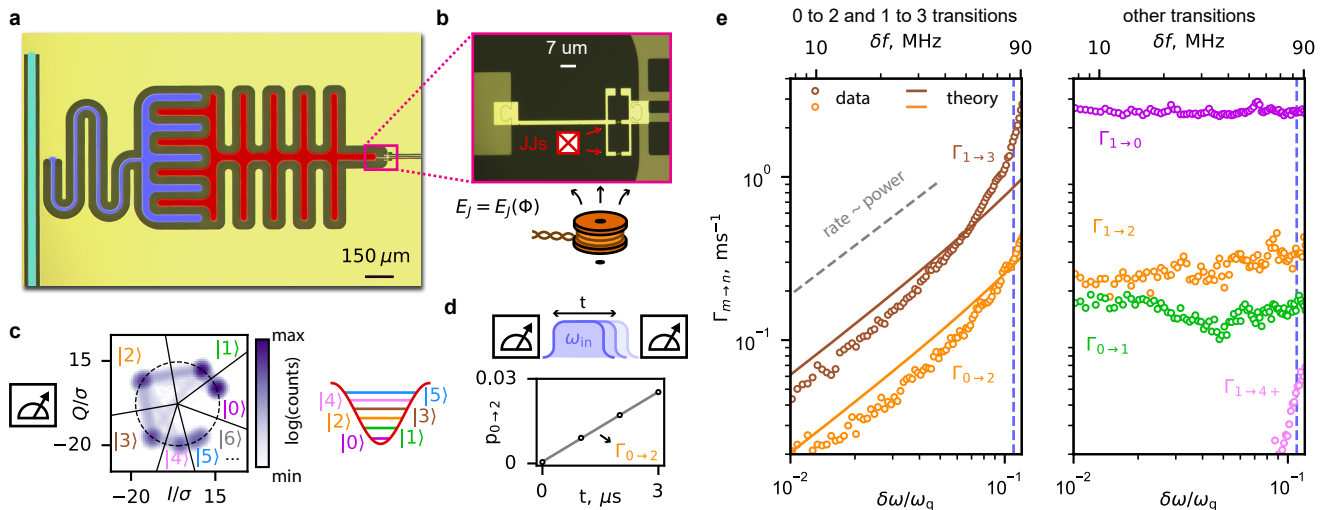


Figure 2. Transition rates of the transmon in the presence of the drive. The qubit is tuned to frequency $\omega_q/2\pi = 758$ MHz (working point of Ref. [5]). The drive frequency $\omega_{in}/2\pi = 9280$ MHz is close to that of the readout resonator, $\omega_{res}/2\pi = 9227$ MHz. (a) False-color microscope image of the device. Quarter-wavelength readout resonator (blue) is capacitively coupled to the transmon island (red). The resonator is inductively coupled to the transmission line (cyan). (b) Zoom-in on the region of the device containing the Josephson junctions. Two Josephson junctions are arranged in a loop. This allows us to tune the frequency of the device by threading magnetic flux through the loop. (c) Single-shot histogram of resonator measurements after intentionally scrambling the state of the transmon with a $\pi/2$ -pulse. The measurement can resolve computational states $|0\rangle$ and $|1\rangle$ as well as the non-computational states $|2\rangle$, $|3\rangle$, $|4\rangle$. All non-computational states higher than $|4\rangle$ are lumped into a single distribution. The population of non-computational states in the histogram stems from transitions caused by inelastic scattering of readout photons. (d) Pulse sequence for rate measurement consists of a pair of measurements separated by a drive pulse of a variable duration and amplitude. We infer the rate by comparing the outcomes for different pulse durations. (e) Transition rates as a function of drive power. The power is quantified by the absolute value of the AC Stark shift experienced by the transmon, $\delta\omega$ (and $\delta f = \delta\omega/2\pi$). The shown range of powers is determined by relevance for qubit readout (see Ref. [5]). Vertical dashed lines show the maximum power level reached by the optimal readout pulse in Ref. [5]. Left panel: the rate of transitions $|0\rangle \rightarrow |2\rangle$ and $|1\rangle \rightarrow |3\rangle$ linearly increases with power. We attribute this to inelastic scattering of readout photons. Solid lines show the prediction of a parameter-free theory, see Eq. (1). Right panel: transition rates $\Gamma_{0\rightarrow 1}, \Gamma_{1\rightarrow 0}, \Gamma_{1\rightarrow 2}$ are roughly power independent. Transitions from $|1\rangle$ to $|4\rangle$ and higher states are strongly suppressed for the range of powers relevant for readout. They appear at highest powers, $\delta\omega/\omega_q \sim 0.1$, but their rate remains small compared to that of other transition channels. The rate of transitions from $|0\rangle$ to states $|4\rangle$ and higher is outside of the plotted range.

sitions without changing the physical picture. After the pulse, we measure the resulting transmon state $|m\rangle$; the measurement can resolve states from $|0\rangle$ to $|4\rangle$, see Figure 2(c,d). Repeating this experiment many times, we find the transition probability between initial state $|m\rangle$ and final state $|n\rangle$. Changing the duration of the pulse yields the transition rates $\Gamma_{m\rightarrow n}$. We then repeat this experiment at different powers of the drive tone. The resulting power-dependence of $\Gamma_{m\rightarrow n}$ is shown in Figure 2(e). The power is quantified by the absolute value of the independently-calibrated AC Stark shift experienced by the transmon, $\delta\omega = \chi\bar{n}$. See supplementary materials for the details of the Stark shift calibration.

At zero drive power, the transitions of the transmon are caused by its coupling to the equilibrium environment. The only non-zero transition rates are $\Gamma_{0\rightarrow 1}$, $\Gamma_{1\rightarrow 0}$, and $\Gamma_{1\rightarrow 2}$. Relaxation rate $\Gamma_{1\rightarrow 0}$ exceeds the excitation rate $\Gamma_{0\rightarrow 1}$ roughly by a factor of 10. This is consistent with the detailed balance relation, $\Gamma_{1\rightarrow 0} = e^{\hbar\omega_q/k_B T}\Gamma_{0\rightarrow 1}$, where $T = 16$ mK is close to the base tem-

perature of our dilution refrigerator. Rates $\Gamma_{0\rightarrow 1}$, $\Gamma_{1\rightarrow 0}$, and $\Gamma_{1\rightarrow 2}$ remain roughly unchanged upon application of a high-power pulse.

Finite drive power excites the transmon to non-computational states. The dominant drive-activated processes that we observe are $|0\rangle \rightarrow |2\rangle$ and $|1\rangle \rightarrow |3\rangle$. The rates of these processes, $\Gamma_{0\rightarrow 2}$ and $\Gamma_{1\rightarrow 3}$, grow linearly with the power of the drive, as long as the power is sufficiently low. The growth becomes faster than linear at higher powers. This drive-induced excitation was the dominant leakage process limiting QND character of our high-frequency readout introduced in Ref. [5]. Direct excitation to states $|4\rangle$ and higher starts to emerge at high drive powers. However, the rate of such excitation remains small compared to $\Gamma_{0\rightarrow 2}$ and $\Gamma_{1\rightarrow 3}$ in the range of powers relevant for readout.

III. INELASTIC SCATTERING THEORY

Previously, readout-induced leakage transitions were attributed to the drive activating accidental multi-excitation resonances in the transmon spectrum [3, 4, 7, 39]. In this process, several readout photons are simultaneously absorbed, promoting the transmon to a non-computational state. This explanation, however, is inadequate for our data. The transitions that we observe do not have a resonant character. Moreover, since $\omega_{\text{res}} \gg \omega_q$, non-linear resonances would excite transmon to much higher non-computational states than $|2\rangle$ or $|3\rangle$. As is shown in Fig. 2(e), excitation to levels $|4\rangle$ and higher does not happen in the range of powers relevant for readout. Thus, an explanation different from transmon multi-excitation resonances is needed for the observed undesired transitions.

We attribute the undesired transitions caused by the readout tone to inelastic scattering of readout photons. As mentioned in the introduction, in the process of inelastic scattering, a readout photon with frequency ω_{in} splits between qubit excitation $|m\rangle \rightarrow |m+2\rangle$ and a photon reflected at a smaller frequency $\omega_{\text{out}} = \omega_{\text{in}} - \omega_{m+2,m}$ [where $\omega_{m+2,m} = (\epsilon_{m+2} - \epsilon_m)/\hbar$, with ϵ_m being the energy of state $|m\rangle$ in the computational basis]. We evaluate the rate of inelastic scattering via Fermi's Golden rule in which we treat the non-linearity as a perturbation. We set out by outlining the outcome of the calculation. We then provide the details of how the calculation is carried out.

According to our calculation, the rate of qubit excitation $|m\rangle \rightarrow |m+2\rangle$ due to the inelastic scattering of readout photons is

$$\Gamma_{m \rightarrow m+2} = (m+1)(m+2) \frac{\omega_q}{\omega_{\text{out}}} \frac{2\pi \text{Re}Z[\omega_{\text{out}}]}{R_Q} \delta\omega. \quad (1)$$

Here, $\delta\omega$ is the previously-introduced AC Stark shift of the qubit; the transition rate scales linearly with this parameter. Quantity $\text{Re}Z[\omega]$ is the dissipative part of the impedance measured between the transmon island and the ground, see Fig. 1(c,f). It is evaluated at the frequency $\omega_{\text{out}} = \omega_{\text{in}} - \omega_{m+2,m}$ of the inelastically scattered photons. The dissipation is enhanced near the frequency of the readout resonator due to the Purcell effect. Detuning ω_{out} from this frequency suppresses the rate of undesired transitions. Constant $R_Q = h/e^2 \approx 25.8 \text{ k}\Omega$ is the resistance quantum.

Next, we compare the calculated rate with our measurement. To this end, we evaluate the impedance $Z[\omega]$ within a lumped model of our circuit depicted in Fig. 1(c) (see supplement [46] for details) and substitute independently measured $\delta\omega$, and ω_q in Eq. (1). The result of this calculation is shown with solid lines in Fig. 2(e). Our parameter-free theory is in a good agreement with the measurement. We attribute the discrepancy of about 25% between the theory and the experiment to our imperfect knowledge of $Z[\omega]$ away from the resonator frequency, see Section IV for further discussion. At the

highest powers, the theory starts to underestimate the measured rate. We believe that this happens due to the activation of the higher-order nonlinear processes. These processes stem from high-frequency modes in the qubit environment. The effects of these modes are explored in Section V.

To derive Eq. (1), we use the Hamiltonian $H = H_t + H_b + V$, modeling the transmon coupled to a transmission line through a readout resonator. The term $H_t = 4E_C(N - n_g)^2 - E_J \cos \varphi$ describes the transmon; N is the Cooper pair number on the island and φ is the superconducting phase. Term $H_b = \sum_k \hbar\omega_k (b_k^\dagger b_k + 1/2)$ describes the transmission line modes labeled by index k ; ω_k and b_k are the corresponding frequencies and annihilation operators, respectively. The term V describes the coupling between the transmon and the transmission line mediated by the readout resonator, $V = \sum_k N(\lambda_k b_k^\dagger + \lambda_k^* b_k)$. In what follows, we link the coupling constants λ_k to the impedance $Z[\omega]$ introduced above.

The core idea of our calculation is to treat transmon non-linearity as a perturbation. First, we diagonalize the Hamiltonian H neglecting the non-linearity [47]. This defines a set of normal modes; the phase operator can be expressed through the normal modes as $\varphi = \varphi_{\text{zpf}}(ia - ia^\dagger) + \sum_k (i\mu_k^* a_k - i\mu_k a_k^\dagger)$. Here, operator a corresponds to the transmon mode dressed by its coupling to the environment; zero-point fluctuations of the transmon phase are given by $\varphi_{\text{zpf}} = (\hbar\omega_q/2E_J)^{1/2}$. In turn, operators a_k correspond to the dressed environment modes. Their participation on the transmon island is described by coefficients $\mu_k = 2\hbar^{-1}\omega_k\lambda_k/(\omega_k^2 - \omega_q^2)$. The nonlinearity couples the normal modes to each other. When $E_J/E_C \gg 1$, the coupling can be captured with a term $-E_J\varphi^4/4!$ obtained by Taylor-expanding the Josephson potential to the fourth order. Applying Fermi's Golden rule with respect to this term, we compute the desired transition rates.

Specifically, we assume that the system is initialized in a state $|\Psi_i\rangle \propto (a_{\text{in}}^\dagger)^{n_{\text{in}}} |\Omega\rangle |m\rangle$, where $|\Omega\rangle$ is the vacuum state of the transmission line and $|m\rangle$ is the state of the transmon; the photon occupation number n_{in} and the mode with frequency ω_{in} characterize the applied drive (index $k = \text{in}$ is used to denote this mode). The final state, where one of the drive photons is inelastically scattered, is $|\Psi_f\rangle \propto (a_{\text{in}}^\dagger)^{n_{\text{in}}-1} a_{\text{out}}^\dagger |\Omega\rangle |m+2\rangle$ (index $k = \text{out}$ denotes the mode to which the drive photon is scattered). The transition rate can be written as

$$\Gamma_{m \rightarrow m+2} = \frac{2\pi}{\hbar} \nu_{\text{out}} |\mathcal{M}_{fi}|^2, \quad \mathcal{M}_{fi} = \langle \Psi_f | E_J \frac{\varphi^4}{4!} | \Psi_i \rangle. \quad (2)$$

Here, ν_{out} is the photon density of states in the transmission line at the frequency ω_{out} .

We compute \mathcal{M}_{fi} by substituting the normal-mode decomposition of the phase operator φ into Eq. (2). We then find

$$\mathcal{M}_{fi} = \sqrt{m+1} \sqrt{m+2} E_C N_{\text{zpf}}^2 \sqrt{n_{\text{in}}} \mu_{\text{in}} \mu_{\text{out}}. \quad (3)$$

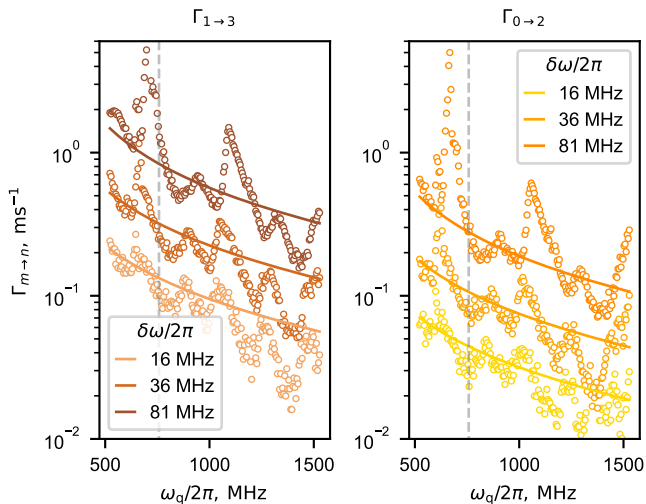


Figure 3. Transition rates $\Gamma_{0 \rightarrow 2}$ and $\Gamma_{1 \rightarrow 3}$ as a function of qubit frequency controlled with flux bias. Both plots show rates measured at three different values of AC Stark shift $\delta\omega$. Grey dashed line indicates the working point of Ref. [5]. Solid lines show the prediction of the inelastic scattering theory, Eq. (1), where $Z[\omega]$ is computed within the lumped element model of the device. The deviations between the theory and experiment stem from two sources. The first is our imperfect knowledge of $Z[\omega]$ away from the resonator frequency (impedance mismatches). The second is higher-order nonlinear processes involving high-frequency modes, see Section V for details.

To express the result in terms of measurable quantities, we note that μ_{in} can be related to the Stark shift as $\delta\omega = \frac{1}{2}\omega_q|\mu_{\text{in}}|^2n_{\text{in}}$ [46]. The constant μ_{out} can be linked to the impedance of the transmon island, $\text{Re}Z[\omega_{\text{out}}]/R_Q = \hbar\omega_{\text{out}}\nu_{\text{out}}|\mu_{\text{out}}|^2/8$. Employing these substitutions in Eqs. (2) and (3) we arrive at Eq. (1).

In our derivation, we assumed that the qubit nonlinearity is weak. In the supplementary materials [46], we show that weak non-linearity assumption can be lifted if the coupling between the transmon and the environment is small. We also develop the theory for other possible inelastic scattering processes. For example, we consider a process where two drive photons and a qubit excitation are converted into an excitation of an environment mode.

IV. INELASTIC SCATTERING RATE VS QUBIT FREQUENCY

Next, to further validate the theory, we measure the rates $\Gamma_{0 \rightarrow 2}$ and $\Gamma_{1 \rightarrow 3}$ at different qubit frequencies. To this end, we repeat the measurement described above at different values of the magnetic flux threaded through the SQUID loop of our device. At each value of the flux we independently calibrate the qubit frequency, the resonator frequency, the relation between the Stark shift

and drive power, and the readout thresholds used for state assignment, see supplementary materials [46].

The results of this measurement for several different drive powers are shown in Fig. 3. At small powers, the theoretical prediction for the rates is close to the data at all qubit frequencies. We attribute the deviations to the impedance mismatches in the transmission line that create an uncertainty in our estimate of $\text{Re}Z$ in Eq. (2). Notably, for a fixed value of the AC Stark shift $\delta\omega$, the rate of unwanted transitions is enhanced at smaller qubit frequencies. The origin of this enhancement is the Purcell effect. Indeed, due to the Purcell effect, $\text{Re}Z[\omega] \propto 1/(\omega - \omega_{\text{res}})^2$. Therefore, $\text{Re}Z[\omega_{\text{out}}] \propto 1/\omega_q^2$ since $\omega_{\text{out}} \approx \omega_{\text{in}} - 2\omega_q$ and ω_{in} is close to ω_{res} . Combined with the prefactor $\propto \omega_q$ in Eq. (2), this results in $\Gamma_{m \rightarrow m+2} \propto \delta\omega/\omega_q$.

At higher drive power additional peaks appear in the measured rates. These stem from the activation of higher-order nonlinear processes involving the spurious device modes. We explore these processes in the next section.

V. FULL CHARACTERIZATION OF TRANSITIONS

The inelastic scattering process that we describe above is only one of the possible mechanisms by which the readout drive can cause unwanted transmon state transitions. In this section, we describe the measurement that reveals the other transition mechanisms. Specifically, we sweep a range of qubit frequencies and drive powers. At each point in this sweep, we measure the transition rates $\Gamma_{m \rightarrow n}$ from the computational states $|m\rangle$ with $m = 0, 1$ to the states $|n\rangle$ with $n = 0, 1, 2, 3, 4+$. Here, $4+$ label any excited non-computational state higher than 3, *i.e.*, states $|4\rangle$, $|5\rangle$, $|6\rangle$ and higher.

The results of this measurement for $m = 1$ are shown in Fig. 4 (similar data for $m = 0$ is presented in the supplementary materials). The plots demonstrate two distinct behaviors for the transition rates. First, rates $\Gamma_{1 \rightarrow 0}$, $\Gamma_{1 \rightarrow 2}$, and $\Gamma_{1 \rightarrow 3}$ have a smooth background present at all qubit frequencies. The background in $\Gamma_{1 \rightarrow 0}$ and $\Gamma_{1 \rightarrow 2}$ is roughly independent of the drive power. Second, there is a set of resonant features in the measured transition rates. These resonances manifest as peaks in the transition rates at certain combinations of qubit frequency and drive power.

For the rate $\Gamma_{1 \rightarrow 0}$, the smooth background corresponds to the direct emission of the qubit excitation into the environment. This process is responsible for the relaxation of the undriven qubit. The rate of qubit decay increases with qubit frequency [46]. The smooth background in $\Gamma_{1 \rightarrow 2}$ corresponds to thermal excitation by the same environment that is responsible for $\Gamma_{1 \rightarrow 0}$. Finally, the smooth background in $\Gamma_{1 \rightarrow 3}$ stems from the inelastic scattering process described in Section III and IV. The rate of this process is zero in the absence of the drive.

Resonant features in the rates $\Gamma_{1 \rightarrow 0}$ (or $\Gamma_{1 \rightarrow 2}$) corre-

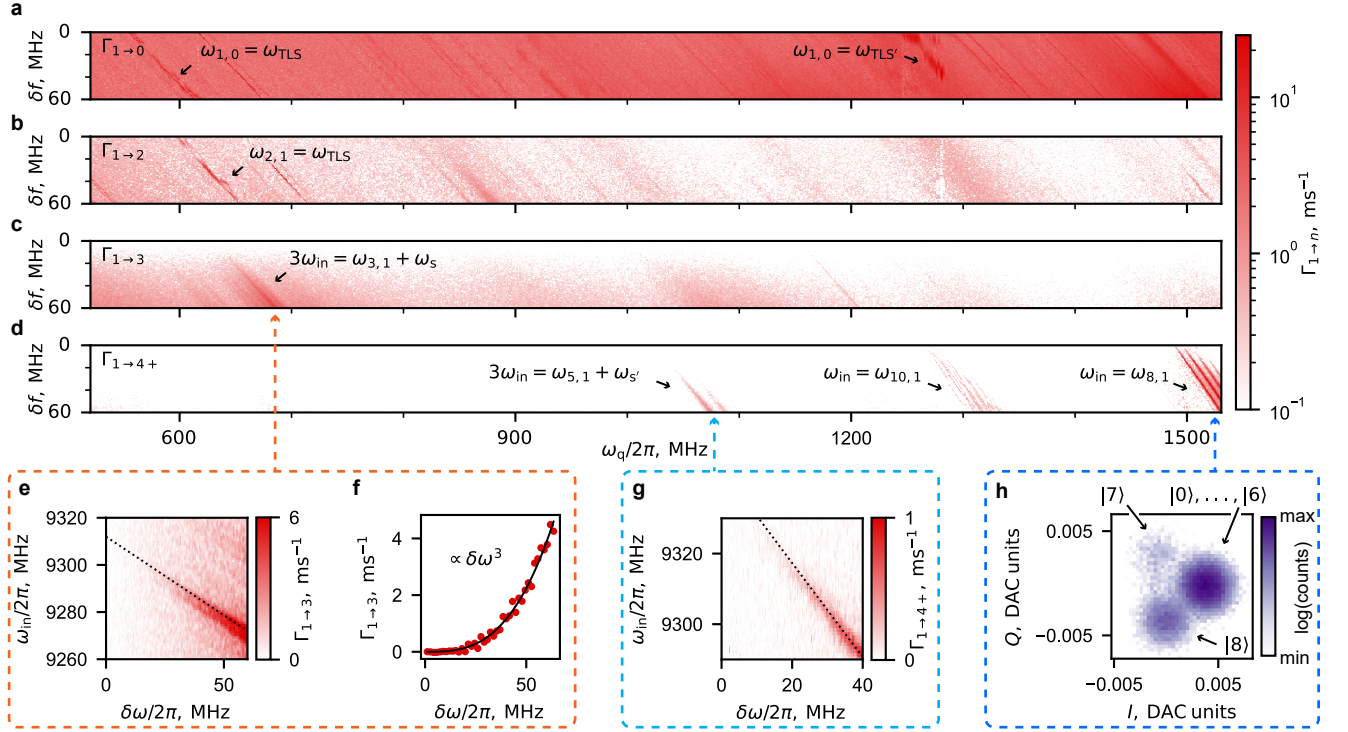


Figure 4. Full characterization of undesired drive-induced transitions of a transmon qubit. (a-d) Transition rates from $|1\rangle$ to various final states plotted as a function of qubit frequency (controlled with magnetic flux) and drive power (quantified by AC Stark shift $\delta f = \delta\omega/2\pi$). The drive frequency $\omega_{\text{in}}/2\pi = 9280$ MHz is close to that of the readout resonator ($\omega_{\text{res}}/2\pi = 9223 - 9240$ MHz depending on the flux). (a,b) Rates $\Gamma_{1 \rightarrow 0}$ and $\Gamma_{1 \rightarrow 2}$. These transitions do not involve the drive photons. The stripey structure is determined by resonances between the AC-Stark shifted qubit frequency and modes in the environment. The frequency shift between the stripes in (a) and (b) is related to difference between $\omega_{1,0}$ and $\omega_{2,1}$ of about $2\pi \cdot 40$ MHz. (c) Rate $\Gamma_{1 \rightarrow 3}$. Smooth background corresponds to the inelastic scattering process described in Fig. 1. Sharp features corresponds to the higher-order inelastic processes [see panels (e) and (f) for details]. (d) Rate $\Gamma_{1 \rightarrow 4+}$ of transitions to $|4\rangle$ and higher states ($|5\rangle$, $|6\rangle$ and higher). These transitions stem either from higher order inelastic processes [see panel (g)] or from activation of multi-excitation resonances in the transmon spectrum [see panel (h)]. The splitting of the transition lines is explained in the main text. (e) The behavior of the sharp feature in $\Gamma_{1 \rightarrow 3}$ at $\omega_q/2\pi = 670$ MHz as a function of the drive frequency ω_{in} and power. Black dashed line corresponds to the condition $3\omega_{\text{in}} = \omega_{3,1}[\delta\omega] + \omega_m$ describing a six-wave mixing process involving a mode with frequency $\omega_m/2\pi = 26.72$ GHz in the qubit environment. (f) The power-dependence of $\Gamma_{1 \rightarrow 3}$ associated with the feature of panel (e). Consistently with the described six-wave mixing process, the rate scales as the cube of power. (g) The behavior of the sharp feature in $\Gamma_{1 \rightarrow 4+}$ at $\omega_q/2\pi = 1070$ MHz as a function of drive-frequency and power. The position of the feature is consistent with condition $3\omega_{\text{in}} = \omega_{5,1}[\delta\omega] + \omega_{m'}$, where $\omega_{m'} = 24.150$ GHz. (h) Reading out the resonator at a lowered frequency allows us to resolve higher excited states of the transmon. The readout histogram shows that the qubit transitions to state $|8\rangle$ after exciting the sharp feature in $\Gamma_{1 \rightarrow 4+}$ at $\omega_q/2\pi = 1500$ MHz.

spond to resonances in the qubit environment at some frequencies ω_{TLS} . Most likely, these resonances originate from excitation (or relaxation) of material defects in the device that are strongly coupled to the qubit degree of freedom [6]. The peaks in $\Gamma_{1 \rightarrow 0}$ occur when a frequency matching condition is fulfilled, $\omega_{1,0}[\delta\omega] = \omega_{\text{TLS}}$. Due to the AC-Stark shift the transition frequency $\omega_{1,0}$ depends on the drive power, $\omega_{1,0}[\delta\omega] = \omega_{1,0}[0] - \delta\omega$. This explains the slope of the resonant features in Fig. 4(a). The peaks in $\Gamma_{1 \rightarrow 2}$ happen when $\omega_{2,1}[\delta\omega] = \omega_{\text{TLS}}$. Frequency $\omega_{2,1}$ differs from $\omega_{1,0}$ due to the qubit anharmonicity. Therefore, the resonant features are shifted by ~ 40 MHz between Fig. 4(a) and Fig. 4(b).

The resonant feature in $\Gamma_{1 \rightarrow 3}$ around 670 MHz stems

from a six-wave process mixing three readout photons with two qubit excitation quanta and a spurious device mode [48]. To determine the number of the involved drive photons, we vary the frequency of the drive and measure the power dependence of the transition rate (the magnetic flux is kept fixed such that in the absence of the drive the qubit frequency is 670 MHz). The result of this measurement is shown in Fig. 4(e). For a fixed amount of AC Stark shift, the position of the resonance depends on the frequency of the drive. The dependence is well described by a resonant condition $3\omega_{\text{in}} = \omega_{3,1}[\delta\omega] + \omega_s$ that corresponds to the six-wave mixing process: absorption of three drive photons with frequency ω_{in} results in the qubit transition $|1\rangle \rightarrow |3\rangle$ and excitation of a spuri-

ous mode with frequency $\omega_s/2\pi = 26.72\text{GHz}$ (likely $3\lambda/4$ mode of the readout resonator). The transition frequency $\omega_{3,1}$ experiences AC Stark shift, $\omega_{3,1}[\delta\omega] = \omega_{3,1}[0] - 2\delta\omega$; this explains the slope in Fig. 4(e). Theoretically, the rate of the described six wave-mixing process is proportional to the cube of the drive power. As is shown in Fig. 4(f), this is indeed the case in our data.

As the qubit frequency is increased, resonant features appear in the rate of excitation to higher excited states of the transmon, $\Gamma_{1\rightarrow 4+}$. The most prominent feature occurs around $\omega_q/2\pi = 1500\text{MHz}$. This “bear claw” feature stems from the activation of a multi-excitation resonance in the transmon spectrum. The drive becomes resonant with the transition between states $|1\rangle$ and $|8\rangle$, *i.e.*, condition $\omega_{\text{in}} = \omega_{8,1}$ is fulfilled. As demonstrated in Fig. 4(h), the drive does indeed excite the transmon to state $|8\rangle$. Notably, the spectroscopic line in Fig. 4(d) is followed by several parallel “replicas”. These replicas stem from the detuning of about 40 MHz between the drive frequency and the frequency of the readout resonator. The replicas correspond to a process in which n drive quanta are converted into a qubit excitation from $|1\rangle$ to $|8\rangle$ and $n - 1$ resonator quanta. They occur when the condition $n\omega_{\text{in}} = \omega_{8,1}[\delta\omega] + (n - 1)\omega_r$ is fulfilled for some integer n .

Some of the other resonant features in Fig. 4 are labeled according to their character. They stem from one of the following mechanisms: (i) direct interaction with isolated lossy modes, (ii) nonlinear processes involving spurious degrees of freedom, (iii) activation of multi-excitation resonances in the transmon spectrum.

VI. DISCUSSION AND CONCLUSION

Applications of superconducting circuits to quantum information tasks require coupling them to microwave tones. In particular, projective measurement of a superconducting qubit is achieved by off-resonantly driving the qubit through a readout resonator. The speed and thus the performance of the measurement can be improved by increasing the drive power. However, the increase of the drive power also leads to the appearance of unwanted state transitions. These drive-activated transitions limit the measurement fidelity. The origin of these transitions is a subject of the present investigation.

In our work, we fully characterize the mechanisms of state transitions in an off-resonantly driven transmon qubit. We focus on the case of a dispersive qubit readout achieved with a readout resonator with a high-frequency, $\omega_{\text{res}}/\omega_q \gg 1$ [5]. By changing the qubit frequency using magnetic flux, we resolve two types of the unwanted drive-activated transitions. Transitions of the first type are ubiquitously present at all qubit frequencies. In their course, the qubit is excited to a non-computational state with a rate proportional to the drive power. These transitions occur due to the inelastic scattering of drive photons back into the readout channel, a process allowed by the transmon non-linearity. Specifically, a drive photon with

frequency ω_{in} splits into a qubit excitation $|0\rangle \rightarrow |2\rangle$ [or $|1\rangle \rightarrow |3\rangle$] and an outgoing photon at a smaller frequency ω_{out} , see Fig. 1. The measured rate of inelastic scattering is in a good agreement with our parameter-free theory, Eq. (1), see Fig. 3. The inelastic scattering process is the dominant source of leakage error in our recent readout result [5].

Transitions of the second type have a resonant character, *i.e.*, they appear at a discrete set of qubit frequencies. The causes of these resonances are excitation of degrees of freedom associated with material defects or spurious electromagnetic modes in the qubit environment. With the increase of transmon frequency, transmon multi-excitation resonances also start to interfere with the readout process. In these resonances, the drive frequency matches that of a transition between a computational and a non-computational state. This leads to leakage from the computational basis.

The understanding developed in our work gives a comprehensive roadmap to mitigating the unwanted drive-induced state transitions in superconducting circuits. Multi-excitation resonances can be suppressed by increasing the drive frequency compared to that of a transmon [5]. Material defects contributing to the spectrum of excitations in the microwave frequency range can potentially be suppressed by improved fabrication techniques. The transitions caused by inelastic scattering of drive photons can be mitigated by means of microwave engineering. For example, the Raman-like process described above can be alleviated by filtering the transmission line at the frequency of inelastically scattered photons ω_{out} .

While detuning of the readout tone from the qubit frequency allows one to increase the readout speed, this route eventually faces limitations due to higher-order inelastic scattering processes. For example, as described in Section V, we observe a strong process where three drive photons convert into two qubit excitations, $|1\rangle \rightarrow |3\rangle$, and an excitation of an electromagnetic mode at $\omega_m/2\pi \approx 27\text{GHz}$. This shows the importance of microwave hygiene even at frequencies far exceeding that of the qubit or of the readout drive.

Finally, we note that inelastic processes involving Bogoliubov quasiparticles can also degrade the performance of superconducting qubit operations carried out with microwave tones. This type of inelastic processes was recently analyzed in Refs. [49, 50].

Note: Recently, two relevant papers appeared [51, 52] that focus on drive-induced transitions caused by multi-excitation resonances.

VII. ACKNOWLEDGEMENTS

We thank Christian K. Andersen, Arno Bargerbos, Marta Pita-Vidal, Lukas Splitthoff, Jaap Westdorp, and Daniel Sank for discussions. We thank Alessandro Miano and Elifnaz Önder for help with the measurement setup. Finally, we thank Y. Sun, K. Woods, L. McCabe, and

M. Rooks for their assistance and guidance in the device fabrication processes.

This research was sponsored by the Army Research Office (ARO) under grants no. W911NF-22-1-0053 and W911NF-23-1-0051, by DARPA under grant no. HR0011-24-2-0346, by the U.S. Department of Energy (DoE), Office of Science, National Quantum Information Science Research Centers, Co-design Center for Quantum Advantage (C2QA) under contract number DE-SC0012704, and by the Air Force Office of Scientific Research (AFOSR) under award number FA9550-

21-1-0209. The views and conclusions contained in this document are those of the authors and should not be interpreted as representing the official policies, either expressed or implied, of the ARO, DARPA, DoE, AFOSR or the US Government. The US Government is authorized to reproduce and distribute reprints for Government purposes notwithstanding any copyright notation herein. Fabrication facilities use was supported by the Yale Institute for Nanoscience and Quantum Engineering (YINQE) and the Yale University Cleanroom. L.F. is a founder and shareholder of Quantum Circuits Inc. (QCI).

-
- [1] A. Y. Kitaev, Fault-tolerant quantum computation by anyons, *Annals of Physics* **303**, 2 (2003).
- [2] A. Kitaev, Anyons in an exactly solved model and beyond, *Annals of Physics January Special Issue*, **321**, 2 (2006).
- [3] D. Sank, Z. Chen, and M. Khezri et al., Measurement-Induced State Transitions in a Superconducting Qubit: Beyond the Rotating Wave Approximation, *Physical Review Letters* **117**, 190503 (2016).
- [4] M. Khezri and A. Opremcak et al., Measurement-induced state transitions in a superconducting qubit: Within the rotating-wave approximation, *Physical Review Applied* **20**, 054008 (2023).
- [5] P. D. Kurilovich, T. Connolly, C. G. L. Bøttcher, D. K. Weiss, S. Hazra, V. R. Joshi, A. Z. Ding, H. Nho, S. Diamond, V. D. Kurilovich, W. Dai, V. Fatemi, L. Frunzio, L. I. Glazman, and M. H. Devoret, [High-frequency readout free from transmon multi-excitation resonances \(2025\)](#), arXiv:2501.09161 [quant-ph].
- [6] T. Thorbeck, Z. Xiao, A. Kamal, and L. C. Govia, Readout-Induced Suppression and Enhancement of Superconducting Qubit Lifetimes, *Physical Review Letters* **132**, 090602 (2024).
- [7] M. F. Dumas, B. Groleau-Paré, A. McDonald, M. H. Muñoz-Arias, C. Lledó, B. D’Anjou, and A. Blais, Measurement-Induced Transmon Ionization, *Physical Review X* **14**, 041023 (2024).
- [8] N. Ofek, A. Petrenko, R. Heeres, P. Reinhold, Z. Leghtas, B. Vlastakis, Y. Liu, L. Frunzio, S. M. Girvin, L. Jiang, M. Mirrahimi, M. H. Devoret, and R. J. Schoelkopf, Extending the lifetime of a quantum bit with error correction in superconducting circuits, *Nature* **536**, 441 (2016).
- [9] Google Quantum AI, Suppressing quantum errors by scaling a surface code logical qubit, *Nature* **614**, 676 (2023).
- [10] V. V. Sivak, A. Eickbusch, B. Royer, S. Singh, I. Tsioutsios, S. Ganjam, A. Miano, B. L. Brock, A. Z. Ding, L. Frunzio, S. M. Girvin, R. J. Schoelkopf, and M. H. Devoret, Real-time quantum error correction beyond break-even, *Nature* **616**, 50 (2023).
- [11] Google Quantum AI, [Quantum error correction below the surface code threshold \(2024\)](#), arXiv:2408.13687 [quant-ph].
- [12] A. A. Clerk, M. H. Devoret, S. M. Girvin, F. Marquardt, and R. J. Schoelkopf, Introduction to quantum noise, measurement, and amplification, *Reviews of Modern Physics* **82**, 1155 (2010).
- [13] A. Blais, R.-S. Huang, A. Wallraff, S. M. Girvin, and R. J. Schoelkopf, Cavity quantum electrodynamics for superconducting electrical circuits: An architecture for quantum computation, *Physical Review A* **69**, 062320 (2004).
- [14] A. Wallraff, D. I. Schuster, A. Blais, L. Frunzio, R.-S. Huang, J. Majer, S. Kumar, S. M. Girvin, and R. J. Schoelkopf, Strong coupling of a single photon to a superconducting qubit using circuit quantum electrodynamics, *Nature* **431**, 162 (2004).
- [15] F. Mallet, F. R. Ong, A. Palacios-Laloy, F. Nguyen, P. Bertet, D. Vion, and D. Esteve, Single-shot qubit readout in circuit quantum electrodynamics, *Nature Physics* **5**, 791 (2009).
- [16] M. D. Reed, L. DiCarlo, B. R. Johnson, L. Sun, D. I. Schuster, L. Frunzio, and R. J. Schoelkopf, High-Fidelity Readout in Circuit Quantum Electrodynamics Using the Jaynes-Cummings Nonlinearity, *Physical Review Letters* **105**, 173601 (2010).
- [17] E. Jeffrey, D. Sank, J. Mutus, T. White, J. Kelly, R. Barends, Y. Chen, Z. Chen, B. Chiaro, A. Dunsworth, A. Megrant, P. O’Malley, C. Neill, P. Roushan, A. Vainsencher, J. Wenner, A. Cleland, and J. M. Martinis, Fast Accurate State Measurement with Superconducting Qubits, *Physical Review Letters* **112**, 190504 (2014).
- [18] T. Walter, P. Kurpiers, S. Gasparinetti, P. Magnard, A. Potočnik, Y. Salathé, M. Pechal, M. Mondal, M. Oppliger, C. Eichler, and A. Wallraff, Rapid High-Fidelity Single-Shot Dispersive Readout of Superconducting Qubits, *Physical Review Applied* **7**, 054020 (2017).
- [19] R. Dassonneville, T. Ramos, V. Milchakov, L. Planat, E. Dumur, F. Foroughi, J. Puertas, S. Leger, K. Bhargava, J. Delaforce, C. Naud, W. Hasch-Guichard, J. Garcia-Ripoll, N. Roch, and O. Buisson, Fast High-Fidelity Quantum Nondemolition Qubit Readout via a Nonperturbative Cross-Kerr Coupling, *Physical Review X* **10**, 011045 (2020).
- [20] F. Swiadek, R. Shillito, P. Magnard, A. Remm, C. Hellings, N. Lacroix, Q. Ficheux, D. C. Zanuz, G. J. Norris, A. Blais, S. Krinner, and A. Wallraff, Enhancing Dispersive Readout of Superconducting Qubits through Dynamic Control of the Dispersive Shift: Experiment and Theory, *PRX Quantum* **5**, 040326 (2024).

- [21] P. A. Spring, L. Milanovic, Y. Sunada, S. Wang, A. F. van Loo, S. Tamate, and Y. Nakamura, [Fast multiplexed superconducting qubit readout with intrinsic Purcell filtering](#) (2024), arXiv:2409.04967 [quant-ph].
- [22] J. Gambetta, W. A. Braff, A. Wallraff, S. M. Girvin, and R. J. Schoelkopf, Protocols for optimal readout of qubits using a continuous quantum nondemolition measurement, *Physical Review A* **76**, 012325 (2007).
- [23] Y. Zhang, B. J. Lester, Y. Y. Gao, L. Jiang, R. J. Schoelkopf, and S. M. Girvin, Engineering bilinear mode coupling in circuit QED: Theory and experiment, *Physical Review A* **99**, 012314 (2019).
- [24] A. Petrescu, M. Malekakhlagh, and H. E. Türeci, Lifetime renormalization of driven weakly anharmonic superconducting qubits. II. The readout problem, *Physical Review B* **101**, 134510 (2020).
- [25] R. Hanai, A. McDonald, and A. Clerk, Intrinsic mechanisms for drive-dependent Purcell decay in superconducting quantum circuits, *Physical Review Research* **3**, 043228 (2021).
- [26] A. Bista, M. Thibodeau, K. Nie, K. Chow, B. K. Clark, and A. Kou, [Readout-induced leakage of the fluxonium qubit](#) (2025), arXiv:2501.17807 [quant-ph].
- [27] R. Lescanne, L. Verney, Q. Ficheux, M. H. Devoret, B. Huard, M. Mirrahimi, and Z. Leghtas, Escape of a Driven Quantum Josephson Circuit into Unconfined States, *Physical Review Applied* **11**, 014030 (2019), publisher: American Physical Society.
- [28] S. Hazra, W. Dai, T. Connolly, P. D. Kurilovich, Z. Wang, L. Frunzio, and M. H. Devoret, [Benchmarking the readout of a superconducting qubit for repeated measurements](#) (2024), arXiv:2407.10934.
- [29] P. Aliferis and B. M. Terhal, Fault-tolerant quantum computation for local leakage faults, *Quantum Info. Comput.* **7**, 139 (2007).
- [30] A. G. Fowler, Coping with qubit leakage in topological codes, *Physical Review A* **88**, 042308 (2013).
- [31] J. Ghosh, A. G. Fowler, J. M. Martinis, and M. R. Geller, Understanding the effects of leakage in superconducting quantum-error-detection circuits, *Physical Review A* **88**, 062329 (2013).
- [32] M. Suchara, A. W. Cross, and J. M. Gambetta, Leakage suppression in the Toric code, *Quantum Info. Comput.* **15**, 997 (2015).
- [33] P. Magnard, P. Kurpiers, B. Royer, T. Walter, J.-C. Besse, S. Gasparinetti, M. Pechal, J. Heinsoo, S. Storz, A. Blais, and A. Wallraff, Fast and Unconditional All-Microwave Reset of a Superconducting Qubit, *Physical Review Letters* **121**, 060502 (2018).
- [34] C. C. Bultink, T. E. O'Brien, R. Vollmer, N. Muthusubramanian, M. W. Beekman, M. A. Rol, X. Fu, B. Tarasinski, V. Ostroukh, B. Varbanov, A. Bruno, and L. DiCarlo, Protecting quantum entanglement from leakage and qubit errors via repetitive parity measurements, *Science Advances* **6**, eaay3050 (2020).
- [35] B. M. Varbanov, F. Battistel, B. M. Tarasinski, V. P. Ostroukh, T. E. O'Brien, L. DiCarlo, and B. M. Terhal, Leakage detection for a transmon-based surface code, *npj Quantum Information* **6**, 1 (2020).
- [36] M. McEwen et al., Removing leakage-induced correlated errors in superconducting quantum error correction, *Nature Communications* **12**, 1761 (2021).
- [37] K. C. Miao and M. McEwen et al., Overcoming leakage in quantum error correction, *Nature Physics* **19**, 1780 (2023).
- [38] R. Shillito, A. Petrescu, J. Cohen, J. Beall, M. Hauru, M. Ganahl, A. G. Lewis, G. Vidal, and A. Blais, Dynamics of Transmon Ionization, *Physical Review Applied* **18**, 034031 (2022).
- [39] X. Xiao, J. Venkatraman, R. G. Cortiñas, S. Chowdhury, and M. H. Devoret, [A diagrammatic method to compute the effective Hamiltonian of driven nonlinear oscillators](#) (2023), arXiv:2304.13656.
- [40] J. Cohen, A. Petrescu, R. Shillito, and A. Blais, Reminiscence of Classical Chaos in Driven Transmons, *PRX Quantum* **4**, 020312 (2023).
- [41] K. N. Nesterov and I. V. Pechenezhskiy, Measurement-induced state transitions in dispersive qubit-readout schemes, *Physical Review Applied* **22**, 064038 (2024).
- [42] Y. Y. Gao, B. J. Lester, Y. Zhang, C. Wang, S. Rosenblum, L. Frunzio, L. Jiang, S. Girvin, and R. J. Schoelkopf, Programmable Interference between Two Microwave Quantum Memories, *Physical Review X* **8**, 021073 (2018), publisher: American Physical Society.
- [43] B. J. Chapman, S. J. de Graaf, S. H. Xue, Y. Zhang, J. Teoh, J. C. Curtis, T. Tsunoda, A. Eickbusch, A. P. Read, A. Koottandavida, S. O. Mundhada, L. Frunzio, M. Devoret, S. Girvin, and R. Schoelkopf, High-On-Off-Ratio Beam-Splitter Interaction for Gates on Bosonically Encoded Qubits, *PRX Quantum* **4**, 020355 (2023).
- [44] Y. Lu, A. Maiti, J. W. O. Garmon, S. Ganjam, Y. Zhang, J. Claes, L. Frunzio, S. M. Girvin, and R. J. Schoelkopf, High-fidelity parametric beamsplitting with a parity-protected converter, *Nature Communications* **14**, 5767 (2023).
- [45] A. Eickbusch, V. Sivak, A. Z. Ding, S. S. Elder, S. R. Jha, J. Venkatraman, B. Royer, S. M. Girvin, R. J. Schoelkopf, and M. H. Devoret, Fast universal control of an oscillator with weak dispersive coupling to a qubit, *Nature Physics* **18**, 1464 (2022).
- [46] See supplementary materials.
- [47] S. E. Nigg, H. Paik, B. Vlastakis, G. Kirchmair, S. Shankar, L. Frunzio, M. H. Devoret, R. J. Schoelkopf, and S. M. Girvin, Black-Box Superconducting Circuit Quantization, *Physical Review Letters* **108**, 240502 (2012).
- [48] S. Singh, G. Refael, A. Clerk, and E. Rosenfeld, [Impact of Josephson junction array modes on fluxonium readout](#) (2025), arXiv:2412.14788 [cond-mat].
- [49] M. Kishmar, P. D. Kurilovich, A. Klots, T. Connolly, I. L. Aleiner, and V. D. Kurilovich, [Quasiparticle-induced decoherence of a driven superconducting qubit](#) (2025), arXiv:2505.00769 [quant-ph].
- [50] S. Chowdhury, M. Hays, S. R. Jha, K. Serniak, T. P. Orlando, J. A. Grover, and W. D. Oliver, [Theory of Quasiparticle Generation by Microwave Drives in Superconducting Qubits](#) (2025), arXiv:2505.00773 [quant-ph].
- [51] M. Fèchant, M. F. Dumas, D. Bénâtre, N. Gosling, P. Lenhard, M. Spiecker, W. Wernsdorfer, B. D'Anjou, A. Blais, and I. M. Pop, [Offset Charge Dependence of Measurement-Induced Transitions in Transmons](#) (2025), arXiv:2505.00674 [quant-ph].
- [52] Z. Wang, B. D'Anjou, P. Gigon, A. Blais, and M. S. Blok, [Probing excited-state dynamics of transmon ionization](#) (2025), arXiv:2505.00639 [quant-ph].